

Selection and Installation of High Resolution Imaging to Monitor the PBFAM Process, and Synchronization to Post-Build 3D Computed Tomography

Jacob P. Morgan, John P. Morgan, Jr., Donald J. Natale, Robert W. M. Smith, Wesley F. Mitchell, Alexander J. Dunbar, Edward W. Reutzel

Applied Research Laboratory, The Pennsylvania State University, P.O. Box 30 State College,
PA 16804

Abstract

Industrial applications of PBFAM continue to expand, and there is a growing interest in the use of sensors to monitor the build process. Sensor data collected during the build process provides insight into process physics and may also lead to a reduction in overall fabrication time and cost by offering an alternative to extensive post-build nondestructive inspection for quality control. Ultimately, sensor data may serve as feedback for real-time control systems that automatically repair flaws before they are buried by subsequent layers.

In this work, high resolution images are explored as a means of monitoring the PBFAM build process inside a 3D Systems ProX320. Key design considerations for camera selection and integration are discussed. Methods and algorithms are developed to calibrate and map layer-wise imagery to laser scan vectors. Images are stacked and exported to standardized 3D data formats to enable easy inspection and comparison to post-build 3D computed tomography (CT) volumes.

1. Introduction

Sensors used to record and monitor the PBFAM build process provide valuable data which supports both research and production methodologies. For research, sensors can be used to better understand process physics and provide a means for research process auditability, verification, and validation. For production, sensors can be used to detect faults in-process and provide a potential feedback pathway for the automatic remediation of defects, thereby saving manufacturing time and expense.

Multiple forms of process monitoring have been explored by other groups. The authors of [1] and [2] used thermal imaging sensors to monitor powder bed fusion (PBF) systems. They were able to correlate thermal distributions with process parameters and provide rudimentary quality control. Optical sensors have also been explored to monitor PBF systems. The authors of [3] combined a digital camera with a pyrometer to study the effects of varying process parameters. In [4] the authors installed a high resolution camera with a tilt shift lens to capture layer wise images in an EOSINT M 270. A comprehensive overview of process monitoring in PBF systems can be found in [5].

For a given build we classify the available data into two categories: design modalities and sensing modalities. A design modality is the data available prior to the build. Examples of design modalities include CAD models and the laser scan vectors that define the path and power of the laser. A sensing modality is any data derived from the real world about the printed geometry. This work focuses on two sensing modalities: high resolution electro-optical (EO) imagery of each layer during the build process and CT volumes taken after the build process. It is not always obvious where flaws are located in the layer-wise imagery, whereas post-build CT allows us to determine where flaws such as voids and unfused powder are located in the final product. Thus, to develop future automated inspection algorithms, the focus of this work is to correlate flaws which are readily detectable in the post-build CT volumes with their exact position and layer in the build imagery. These correlated features form a labeled dataset of positive defect examples which can be used to support future automatic fault detection algorithms built using Machine Learning techniques.

For this work all builds were completed on a 3D Systems Prox320 powder bed fusion additive manufacturing system outfitted with a Nikon D810 camera. Post-build analysis was completed with a GE phoenix v|tome|x m CT scanner. To start, imaging system components must be selected to achieve a high spatial resolution while keeping the entire ProX320 build area in focus. We achieve this using a tilt-shift lens and choose the lighting to produce images with varying contrast to highlight problematic features within the build area. After collecting the layer-wise build imagery and the post-build CT volumes, each sensing modality is registered to a common coordinate frame of reference to allow for cross modality comparison. Registered data is stored in a 3D DICOM data format, which contains the coordinate frame of reference and can be read and reviewed using widely available DICOM viewer software.

Section 2 of this paper discusses the design, selection, and configuration of imaging components to capture in-process layer-wise build imagery. Camera position, lens choice, lighting, and mounting considerations are discussed. Section 3 presents algorithms for registering layer-wise imagery to laser vectors and for registering CT volumes to laser vectors. Some additional detail is also provided on the DICOM file format used. Section 4 presents qualitative results for four parts and a quantitative analysis of the CT to laser vector registration error. Section 5 offers some conclusions and directions for future work.

2. Camera Selection, Imaging, and Integration Considerations

The ProX320 includes two viewing windows at the top of the process chamber through which the build surface can be captured with a camera. Figure 1 shows a cross-sectional view of the process chamber with the camera mounted at one of the top viewports. It is desirable to keep the camera out of the processing environment; however, this introduces a minimum stand-off from the build surface and an off-normal viewing angle because the laser optics occupy the area directly above the build plate. Lights are placed as close to the build area as possible in locations that do not interfere with the recoater as suggested by the manufacturer. With these constraints, the goal is to capture the entire build plate area (275mm x 275mm) at the highest resolution possible.

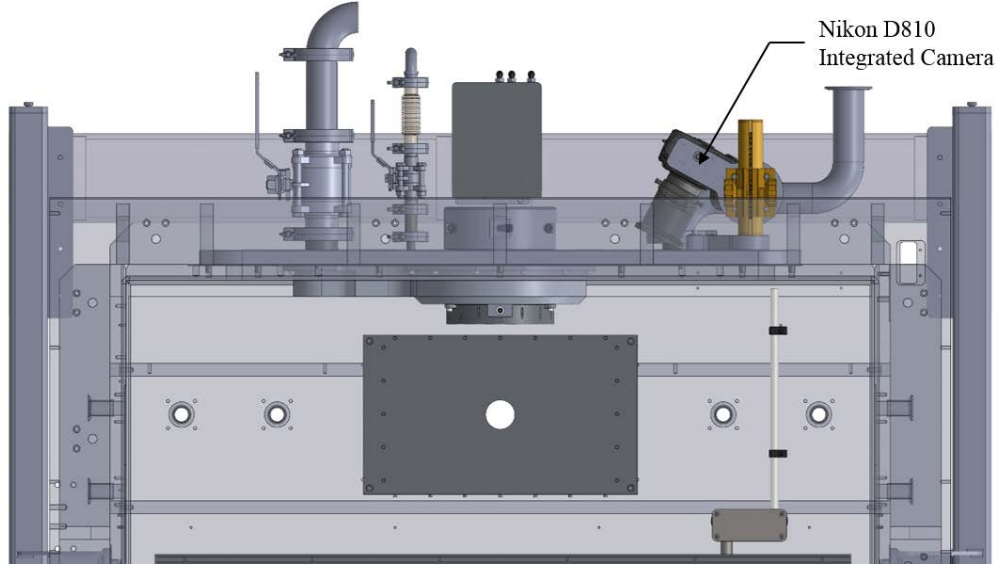


Figure 1: Illustration of the 3D Systems ProX 320 process chamber with the integrated camera.

The image resolution is the physical size of a pixel, which at the center of the image is the size of a single detector on the camera sensor divided by the magnification. Let f be the focal length and s be the object distance. The magnification may then be approximated using the Gaussian lens equation [6]

$$M = \frac{f}{s - f} \quad (1)$$

Because the optical axis of the camera is off-normal, the plane that can be perfectly focused cannot be made coincident with the build surface. Thus, in addition to resolution, we must also consider how much of the build area is within the depth of field. The depth of field is the region between the nearest object distance D_{near} and furthest object distance D_{far} that appears sharp in the image. A point that is out of focus will appear as a blur in the image whose sharpness is quantified by the diameter of the blur on the sensor. Ideally we would like this to be less than the detector size, which is the physical size of an imaging element on the sensor array. To calculate the depth of field, we first define the hyperfocal distance H

$$H = \frac{Df}{d} + f \quad (2)$$

where D is the aperture diameter and d is the detector size. D_{near} and D_{far} are then

$$D_{near} = s \left(\frac{H - f}{H + s - 2f} \right) \quad (3)$$

$$D_{far} = s \left(\frac{H - f}{H - s} \right) \quad (4)$$

To maximize the depth of field, we would like to minimize D_{near} and maximize D_{far} . Since the object distance s is fixed, analysis of equations (2), (3), and (4) reveals three options for improving the depth of field: decrease the aperture diameter, decrease the focal length, or increase the detector size. However, each of these solutions has a tradeoff. Decreasing the aperture diameter reduces light input to the camera, which means more ambient light is required. Additionally, as the aperture diameter becomes too small the camera becomes diffraction limited [6]. Decreasing the focal length will decrease the magnification in equation (1), which lowers the resolution. Increasing the detector size will also lower the resolution.

A better approach is to tilt the plane of focus so that it is parallel to the build surface using a tilt-lens. Nikon sells several perspective control lenses at fixed focal lengths, which have the capability to tilt and shift perpendicular to the plane of tilt. Here we use the “PC-E Micro NIKKOR 45mm f/2.8D ED” lens. Figure 2 shows the mounting of the Nikon D810 and lens. Focusing the build area is complicated because adjusting the focus changes the angle of the plane of focus, and calculating the exact values is not possible because we do not have a model of the lens that accounts for the focus feature. Thus, an iterative process of adjusting focus distance and tilt was used to get the desired image via trial and error.

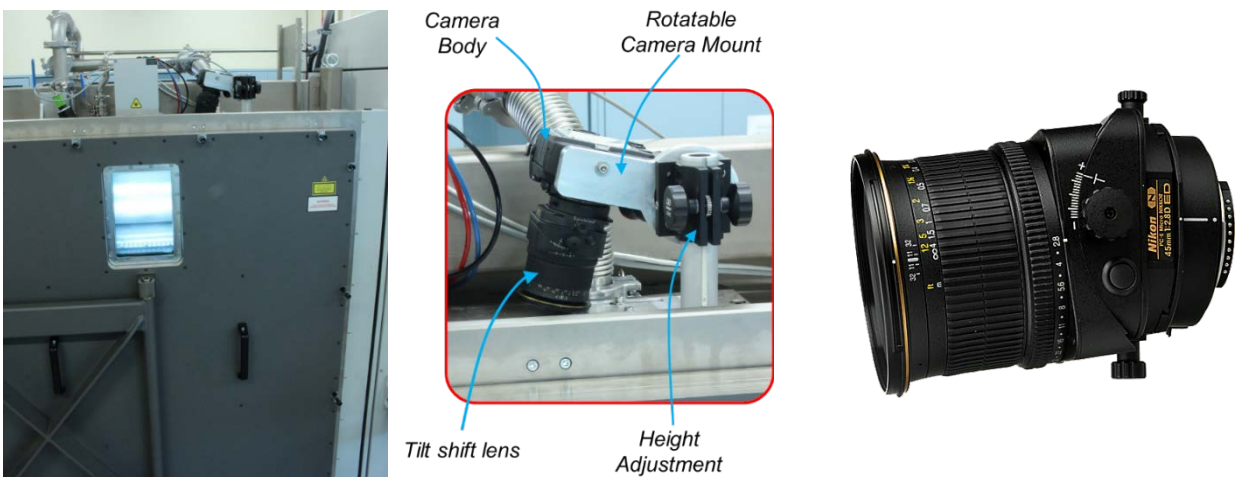


Figure 2: External mounting of Nikon D810 with PC-E Micro NIKKOR 45mm f/2.8D ED lens. The shift capability is not used.

Figure 3 shows a representative depth of field for our camera and lens when the tilt is set to zero. The lens center has been placed at its approximate location on the build chamber, the optical axis is 30° off-normal, and the aperture diameter is $f/32$. The thick line at the bottom is the 275mm build plate and it can be seen that even at the smallest aperture diameter the depth of field does not cover the entire area.

Figure 4 shows the same scenario as figure 3, but with the image plane tilted at an angle α with respect to the lens plane such that the plane of focus is coincident with the build surface. For the approximate camera model shown, α can be found using the Scheimpflug principle [7]. This states that the image plane, lens plane, and plane of focus all intersect at a line, which is denoted by S in figure 4 (shown as a point because the line is perpendicular to the image). Also note that the depth of field is now a wedge with the D_{near} and D_{far} planes intersecting at the hinge line P .

However, since we are imaging a plane, the depth of field no longer matters and the aperture diameter may be set to a larger value. Larger aperture diameters let in more light, which increases the signal to noise ratio of the image.

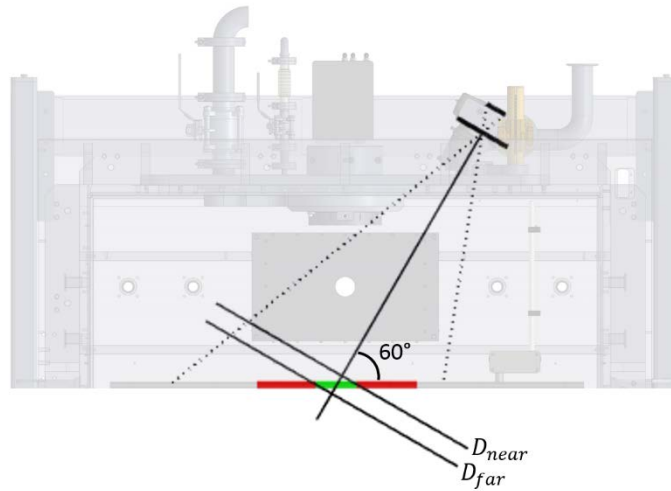


Figure 3: Depth of field with 0° tilt. i.e. conventional image

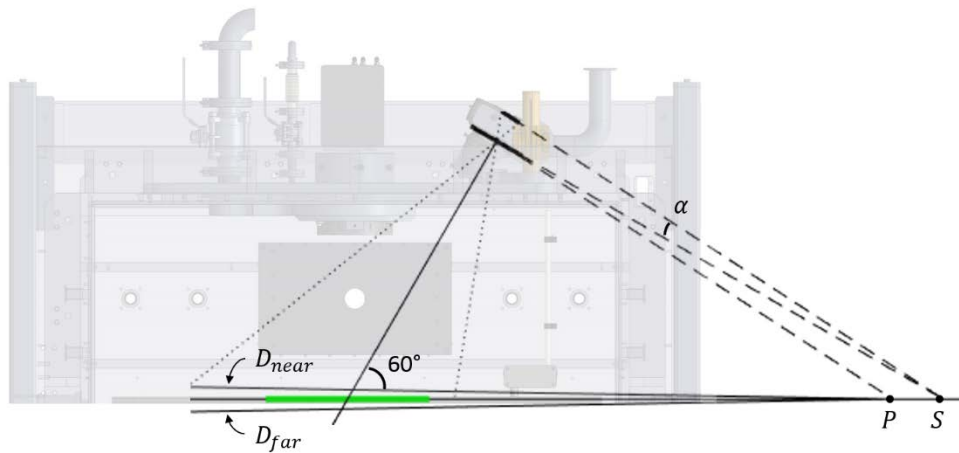


Figure 4: Depth of field with tilt α such that the plane of focus coincides with the build plate. i.e. tilt introduced

3. Registering Laser Vectors, Imagery, and CT

To locate the same point in space across all of the sensing modalities, they must all be registered to a common coordinate frame of reference. An ideal choice is to align the sensing modalities to a design modality because the design modalities have no measurement error. If we were to directly align sensing modalities, the measurement error in each would be compounded. In this work we use the laser scan vectors as the coordinate frame of reference because they directly correspond to the content of the build imagery. Section 3.1 discusses how to align the build images to the laser vectors, and section 3.2 discusses how to align the CT volume to the laser vectors. Figure 5 shows the laser vectors, a layer-wise build image, and the CT volume for the part used as an example in this section.

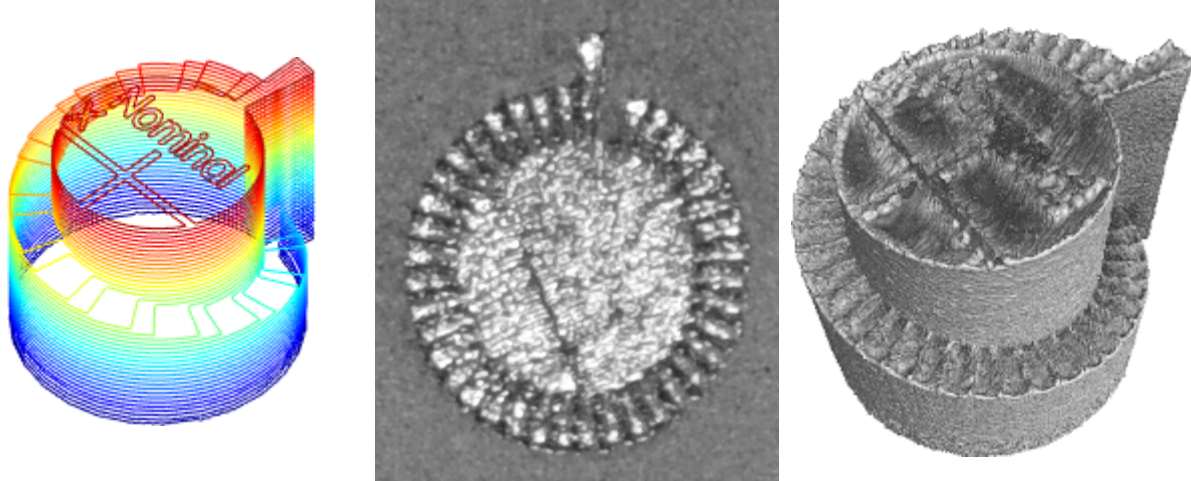


Figure 5: Exterior contours of the laser vectors every 10 layers (left), build image for layer 147 (middle), and post-build CT volume (right). Cylinder diameter is approximately 10 mm.

After registration of the data modalities to a common coordinate frame of reference, we store each modality using the DICOM file format because of the convenient properties for representing 3D data and the wide availability of viewers. The DICOM format [8] defines several Information Object Definitions (IODs) that specify which information in the metadata is required and which is optional. In order to store the 3D position of an image we require the image plane module, which is contained in the following IODs: computed tomography image (CT), magnetic resonance image (MR), and positron emission tomography image (PET). We use the CT IOD for every modality because the CT volume is already in this format. Table 1 shows the relevant metadata for referencing the image in 3D.

Table 1: DICOM metadata for referencing the 3D image location contained within the CT IOD.

Metadata	Description
PixelSpacing	Physical [height, width] of each pixel in mm.
ImageOrientationPatient	The orientation with respect to the build surface defined as x,y,z of the row axis followed by x,y,z of the column axis.
ImagePositionPatient	The x,y,z coordinate of the center of the upper left hand pixel in mm.
SliceThickness	Nominal slice thickness in mm.
SliceLocation	Relative position of the image plane in mm.

3.1 Build Image to Laser Vector Registration

Due to mounting constraints in the system, the image plane of the camera is not parallel to the build surface. However, because the build surface is a plane, this difference can be modeled by a planar homography [9]. This means we can transform the perspective of the layer-wise build imagery to a dimensionally accurate top-down view. Typically a separate calibration procedure is required to determine the homography where a known geometry target, such as a checkerboard, is placed at the plane being corrected. The homography can then be computed from the image of this known geometry. However, this calibration technique poses a few problems in our application

because it is difficult to position a checkerboard exactly at the build surface and if the camera or lens elements move even slightly between builds, the calibration is no longer valid. Fortunately, we can circumvent the use of a geometry target because there is already a known geometry present in the images: the fused material that corresponds with the laser vectors. The remainder of this section will discuss how to directly optimize the homography using the layer-wise build images and the laser vectors.

Let $\bar{x} \in \mathbb{R}^3$ be a coordinate in the image frame of reference and $\bar{x}' \in \mathbb{R}^3$ be the transformed coordinate in the vector frame of reference where the overbar denotes a homogeneous coordinate. To convert a homogeneous coordinate to a 2D coordinate, we define a projection

$$\begin{aligned}\bar{x} &= [wu \quad wv \quad w]^T \\ x &= \text{proj}(\bar{x}) = [u \quad v]^T.\end{aligned}\tag{5}$$

Let $H \in \mathbb{R}^{3 \times 3}$ be the homography that transforms coordinates in the image frame of reference to the laser vector frame of reference. Then

$$\begin{aligned}H &= \begin{bmatrix} h_{11} & h_{12} & h_{13} \\ h_{21} & h_{22} & h_{23} \\ h_{31} & h_{32} & 1 \end{bmatrix} \\ \bar{x}' &= H\bar{x}.\end{aligned}\tag{6}$$

Note that because homogeneous coordinates are invariant to scale, h_{33} can be defined as unity. Thus we only need to optimize the eight remaining homography coefficients. This can be done using the Levenberg-Marquardt algorithm [10], and to improve runtime we use an inverse compositional approach [11]. Here we will present the cost function to be minimized and the Jacobian matrix of first derivatives required for analytic update equations.

For optimization we use a direct image alignment approach [11] where the images are such that there is a high intensity over fused metal and a low intensity over powder. In the build images, this is achieved using a standard deviation filter. The fused material has a large standard deviation due to the various reflections, whereas the powder intensities are normally distributed with a low standard deviation. Note that because there is some window size associated with the filter, the high intensity values in the filtered image extend beyond the bounds of the part. Figure 6 shows a build image before and after filtering.

Next we need to create a synthetic image from the laser vectors, subsequently referred to as the exemplar. We start by rasterizing the vectors into a binary image. While the binary image could be used directly, the alignment would be poor because the filtered build images have some dilation due to the standard deviation filter size. To create a better match, the binary 1s in the synthetic image are replaced by white noise and the new image is filtered in the same way as the build images. Figure 7 shows the exemplar before and after filtering.

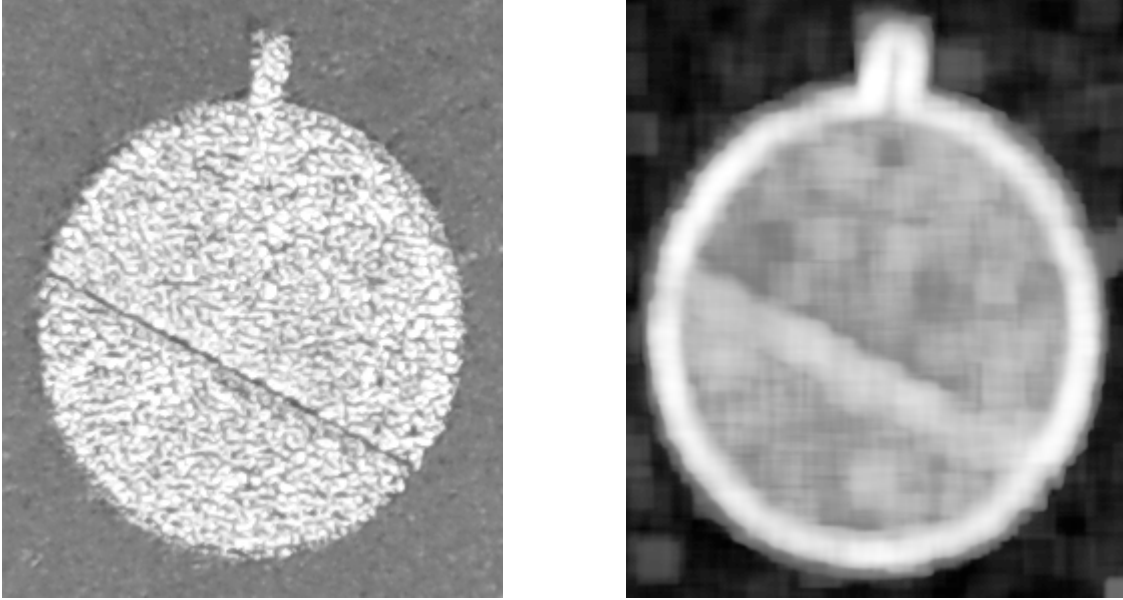


Figure 6: Sample high resolution image (left) and image filtered using a standard deviation filter (right).

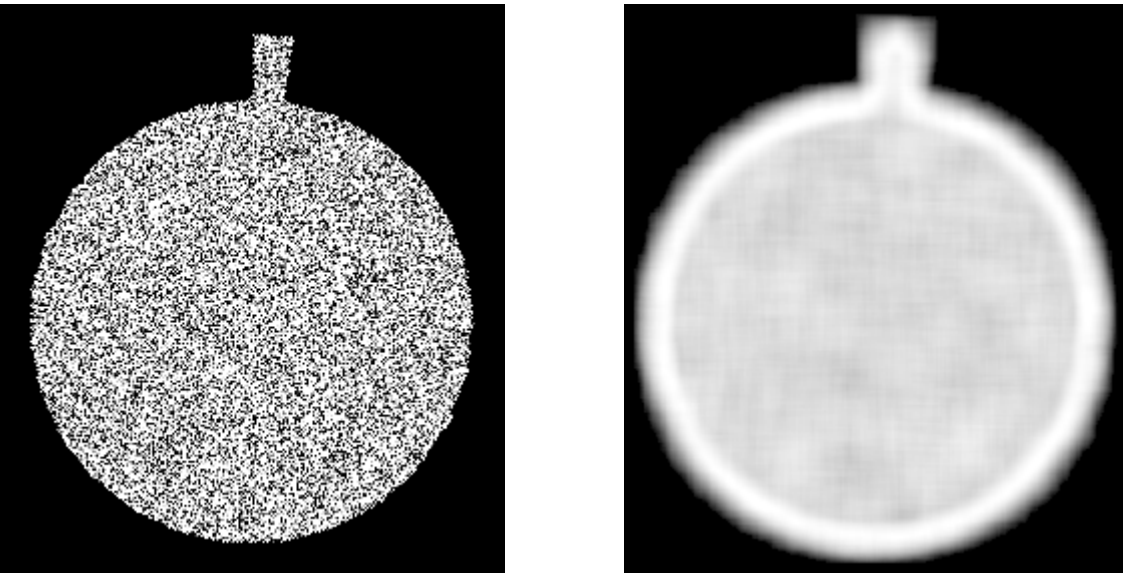


Figure 7: Binary image with added white noise (left) and generated exemplar from standard deviation filter (right).

Let I_B be the filtered build image and I_E be the exemplar image generated from the laser vectors. The idea is that when these two images are aligned, the difference between them will be minimized. Thus, the goal is to iteratively minimize the sum of squared differences with respect to an update ΔH to the homography

$$e^{(k+1)} = \min_{\Delta H} \frac{1}{2} \sum_i \left(I_E(\text{proj}(\Delta H \bar{x}_i)) - I_B(\text{proj}(H^{(k)} \bar{x}_i)) \right)^2 \quad (7)$$

$$H^{(k+1)} = H^{(k)} (\Delta H)^{-1} \quad (8)$$

where the superscript in parenthesis indicates the iteration number. This is referred to as the inverse compositional approach because we calculate an update for the vector coordinates and then apply the inverse of that update to the build image coordinates. We initialize $H^{(0)}$ by having the user select four point correspondences as outlined in chapter 4 of [9], but a prior calibration could also be used.

To minimize the error $e^{(k+1)}$, the derivative with respect to ΔH is set to zero. Here we will show how to calculate the derivative and refer the reader to [10] for implementing the Levenberg-Marquardt algorithm. Applying the chain rule

$$\left. \frac{de_i^{(k)}}{d\Delta H} \right|_{\Delta H=I} = \left(I_E(x_i) - I_B \left(\text{proj}(H^{(k)} \bar{x}_i) \right) \right) \nabla I_E(x_i)^T \left(\left. \frac{d\text{proj}(\Delta H \bar{x}_i)}{d\Delta H} \right|_{\Delta H=I} \right) \quad (9)$$

$$\left. \frac{d\text{proj}(\Delta H \bar{x}_i)}{d\Delta H} \right|_{\Delta H=I} = \begin{bmatrix} u_i & v_i & 1 & 0 & 0 & 0 & -u_i^2 & -u_i v_i \\ 0 & 0 & 0 & u_i & v_i & 1 & -u_i v_i & -v_i^2 \end{bmatrix} \quad (10)$$

where u_i and v_i are the column and row of the exemplar image coordinate. The last two terms of (9) form the Jacobian $J_i \in \mathbb{R}^{1 \times 8}$ of a single coordinate, which can be stacked into the full matrix $J \in \mathbb{R}^{n \times 8}$ required for the Levenberg-Marquardt algorithm. Note that J_i is independent of $H^{(k)}$, which means it is constant across iterations and can be pre-computed. This is the advantage of using inverse composition.

To accommodate large differences between the exemplar and build image, we employ an image pyramid. At each level of the pyramid the image resolution is down-sampled by a factor of two. The optimization is then performed on each level starting at the lowest resolution image and using the result of each level to initialize the next level. In the low resolution images large differences are small enough to be optimized, and with successive layers the precision of the alignment is refined.

3.2 CT to Laser Vector Registration

The CT volume is a 3D grid of voxels where each voxel stores the part density at its location, thus the part can be thresholded by extracting the high density voxels. The thresholded part then corresponds to the stacked laser vector layers. However, the CT volume may be collected at any orientation, so we must determine the rotation $R \in \mathbb{R}^{3 \times 3}$ and translation $t \in \mathbb{R}^3$ that best align the CT volume to the stacked laser vectors. The combination of a rotation and translation is referred to as a rigid transformation.

Let $\bar{X} \in \mathbb{R}^4$ be a coordinate in the CT frame of reference and $\bar{X}' \in \mathbb{R}^4$ be the transformed coordinate in the laser vector frame of reference where the overbar denotes a homogeneous coordinate. To convert a homogeneous coordinate to a 3D coordinate, we define a projection

$$\begin{aligned}\bar{X} &= [wx \quad wy \quad wz \quad w]^T \\ X &= \text{proj}(\bar{X}) = [x \quad y \quad z]^T\end{aligned}\tag{11}$$

Let $T \in \mathbb{R}^{4 \times 4}$ be the rigid transformation that transforms voxel coordinates in the CT frame of reference to the laser vector frame of reference. Then

$$\begin{aligned}T &= \begin{bmatrix} R & t \\ 0 & 1 \end{bmatrix} \\ \bar{X}' &= T\bar{X}\end{aligned}\tag{12}$$

For optimization we require a minimal representation, and here we use the Lie algebra [12]. Let $(\omega \in \mathbb{R}^3, v \in \mathbb{R}^3)$ be an element of the Lie algebra that can be exponentially mapped to a rigid transformation. It is reasonable to assume that the rotational updates will be small, and we can therefore simplify the exponential mapping with a small angle assumption to get

$$\begin{aligned}T &:= \exp\left(\begin{bmatrix} \omega \\ v \end{bmatrix}\right) \cong \begin{bmatrix} I + [\omega]_{\times} & \left(I + \frac{1}{2}[\omega]_{\times}\right)v \\ 0 & 1 \end{bmatrix} \\ [\omega]_{\times} &= \begin{bmatrix} 0 & -\omega_3 & \omega_2 \\ \omega_3 & 0 & -\omega_1 \\ -\omega_2 & \omega_1 & 0 \end{bmatrix}\end{aligned}\tag{13}$$

During optimization, updates are calculated as an element of the Lie algebra and then mapped to a rigid transformation matrix to be accumulated.

A common approach for aligning 3D points is the iterative closest point algorithm (ICP) [13], which iteratively minimizes the distance between nearest neighbors in each set of points. In this scenario we would align a uniform sampling of the surface of the CT volume to a uniform sampling of exterior contours of the laser vector layers. However, it is difficult to uniformly sample the laser vectors because the x,y resolution is much higher than the z resolution and it is non-trivial to interpolate points between layers. We have found that a better approach is to convert the laser vectors to a truncated signed distance function (TSDF) and align the CT surface points to the TSDF [14].

A TSDF is a grid of voxels where the value at each voxel is the distance to the nearest surface. Voxels inside the part are given negative distance and voxels outside the part are given positive distance. The surface of the part is implicitly defined where the distance is zero, which is well defined as where the distance changes sign. To initialize the TSDF volume we create a raster for each laser vector layer, calculate the true 2D distance of every raster pixel to the nearest vector, and stack these rasters into a 3D volume. Next we run the fast sweeping algorithm [15] to get the 3D distance. Figure 8 shows a few slices of a TSDF.

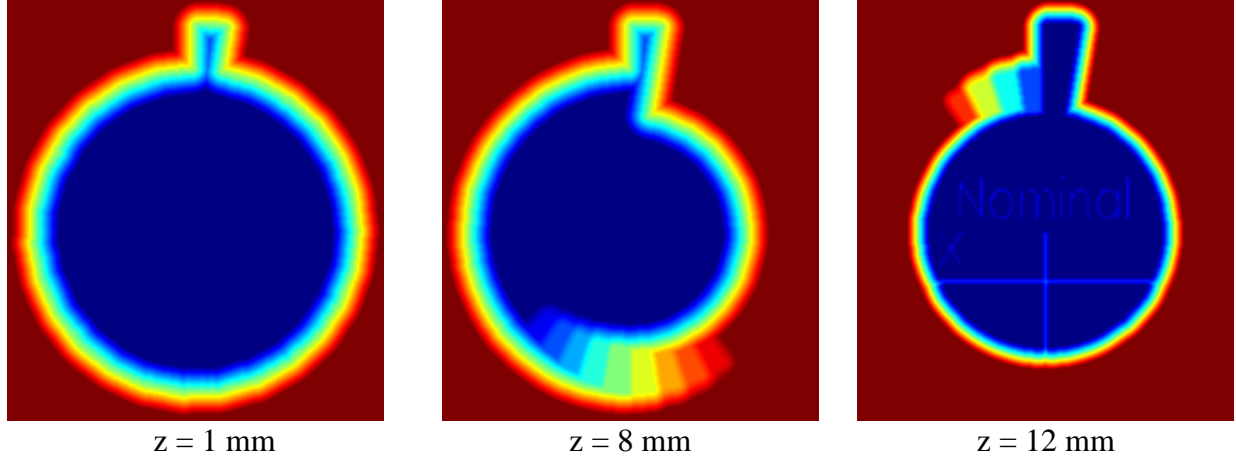


Figure 8: Truncated signed distance function sliced in the x-y plane at varying z-positions. Red indicates positive distance and blue indicates negative distance.

Let $\Psi(X)$ denote the distance at X in the TSDF generated from the laser vectors. The idea is that when the CT surface points are aligned to the TSDF, the distance at each point will be small. Thus, the goal is to iteratively minimize the sum of squared distances with respect to an update $(\Delta\omega, \Delta v)$ to the rigid transformation

$$e^{(k+1)} = \min_{\Delta\omega, \Delta v} \frac{1}{2} \sum_i \Psi \left(\text{proj} \left(\exp \left(\begin{bmatrix} \Delta\omega \\ \Delta v \end{bmatrix} \right) T^{(k)} \bar{X}_i \right) \right)^2 \quad (14)$$

$$T^{(k+1)} = \exp \left(\begin{bmatrix} \Delta\omega \\ \Delta v \end{bmatrix} \right) T^{(k)} \quad (15)$$

where the superscript in parenthesis indicates the iteration number. We initialize $T^{(0)}$ by having the user select three point correspondences and running absolute orientation [16]. Alternatively, a CT analyst could roughly orient the CT volume to match the orientation on the build surface, in which case $R^{(0)} = I$ and $t^{(0)}$ is obtained by aligning the centroid of the thresholded part with the centroid of the laser vectors.

As with the build images, to minimize $e^{(k+1)}$ we set the derivative with respect to $(\Delta\omega, \Delta v)$ to zero. Here we will show how to calculate the derivative and refer the reader to [10] for implementing the Levenberg-Marquardt algorithm. Applying the chain rule

$$\left. \frac{de_i^{(k)}}{d\Delta\omega, \Delta v} \right|_{\Delta\omega, \Delta v=0} = \Psi(X_i^{(k)}) \nabla \Psi(X_i^{(k)})^T \left(\left. \frac{d\text{proj} \left(\exp \left(\begin{bmatrix} \Delta\omega \\ \Delta v \end{bmatrix} \right) \bar{X}_i^{(k)} \right)}{d\Delta\omega, \Delta v} \right|_{\Delta\omega, \Delta v=0} \right) \quad (16)$$

$$\left. \frac{d\text{proj} \left(\exp \left(\begin{bmatrix} \Delta\omega \\ \Delta v \end{bmatrix} \right) \bar{X}_i^{(k)} \right)}{d\Delta\omega, \Delta v} \right|_{\Delta\omega, \Delta v=0} = \begin{bmatrix} 0 & z_i^{(k)} & -y_i^{(k)} & 1 & 0 & 0 \\ -z_i^{(k)} & 0 & x_i^{(k)} & 0 & 1 & 0 \\ y_i^{(k)} & -x_i^{(k)} & 0 & 0 & 0 & 1 \end{bmatrix} \quad (17)$$

where $\bar{X}_i^{(k)} = T^{(k)}\bar{X}_i$ and $x_i^{(k)}$, $y_i^{(k)}$, and $z_i^{(k)}$ are the coordinates of $X_i^{(k)}$. The last two terms of (16) form the Jacobian $J_i \in \mathbb{R}^{1 \times 6}$ of a single point, which can be stacked into the full matrix $J \in \mathbb{R}^{n \times 6}$ required for the Levenberg-Marquardt algorithm. In this case we must re-compute the Jacobian at each iteration.

4. Results and Discussion

To analyze how accurately a CT point can be located in the layer-wise build imagery, we examine the error for each registration separately. Section 4.1 discusses the build image registration in detail, and Section 4.2 discusses the CT volume registration in detail. Because the build imagery and CT volume are registered to the same coordinate frame of reference, they are implicitly registered to each other. Figure 9 shows a point denoted by a green marker that has been located in each modality of the parameter cylinder from Section 3. We may approximate the CT volume to build image error as the sum of the build image to laser vector error and the CT volume to laser vector error.

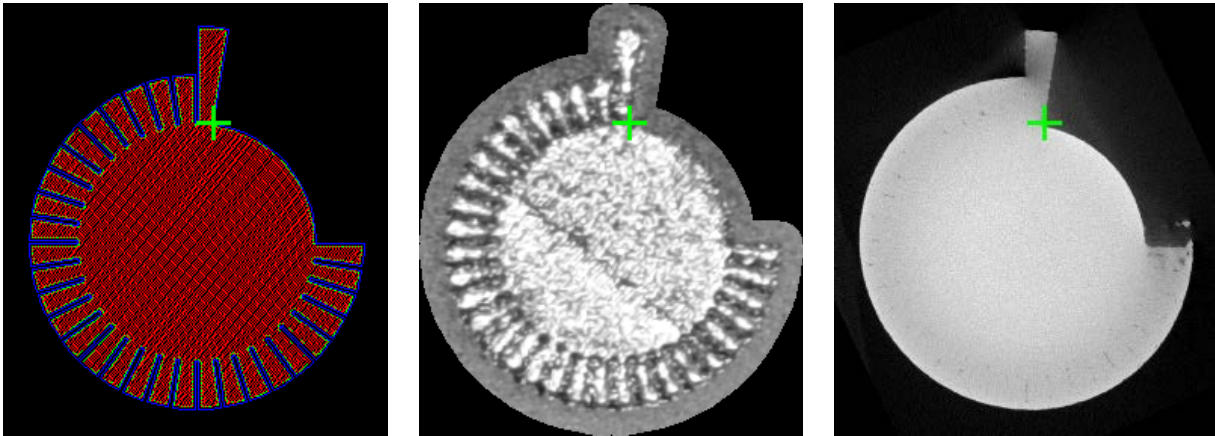


Figure 9: Registered DICOM images for the nominal parameter cylinder: rasterized laser vectors (left), build image (middle), and CT data (right). In the rasterized laser vectors, contours are indicated by the blue lines and hatching is indicated by the red lines. The green marker is located at the same position in each image.

Results are presented for four parts: the Nominal Parameter Cylinder, the V+20 Parameter Cylinder, the O2 Fin, and the L2 Fin. The parameter cylinders are vertical cylinders with a spiral staircase around the exterior and a single large fin to eliminate rotational ambiguity. The fins are thin walls printed upwards at a 45° angle to their base. Each part has one CT volume and build images collected both before and after the laser scan with front, side, and top lighting for a total of six views. Figure 10 shows each view for one layer of the nominal parameter cylinder. Images are taken prior to the laser scan because it is thought that anomalies in the powder layer may correspond to defects within the part. Images are taken at various lighting angles because different surface perturbations can be highlighted [17].

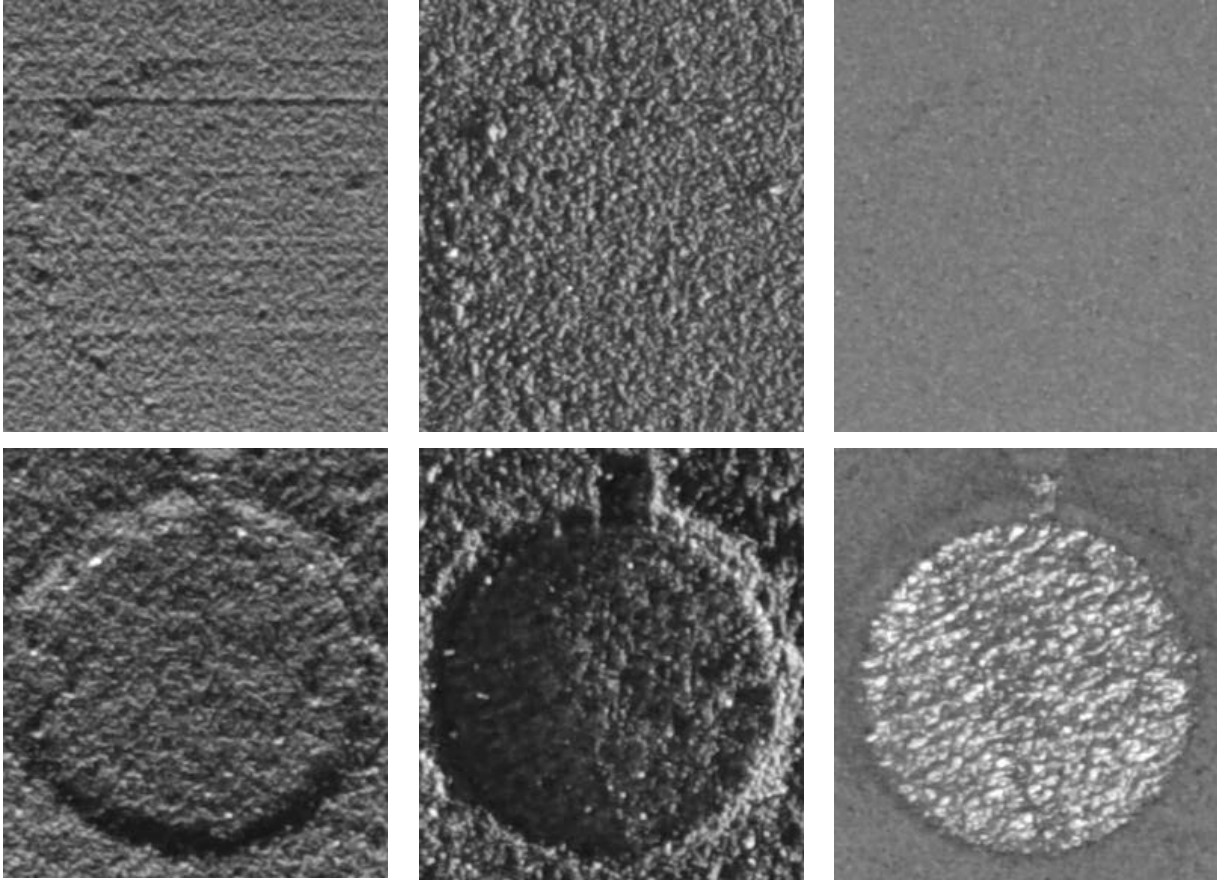


Figure 10: Images captured for nominal parameter cylinder pre laser scan (top) and post laser scan (bottom). Three different lighting directions are used: front (left), side (middle), and top (right). Cylinder diameter is approximately 10 mm.

The resolution of the uncorrected image varies across the build surface because it is viewed at an angle, whereas the resolution of the perspective corrected image is consistent across the build surface. For the perspective corrected images, we chose to set the resolution equal to the uncorrected image resolution at the center of the build plate. Using the Nikon D810 with a PC-E Micro NIKKOR 45mm f/2.8D ED lens we obtained an image resolution of approximately $62.5\mu\text{m}$ per pixel. From visual inspection of images such as figure 11, 12, 13, and 14 (left) we estimate that the build image registration is accurate to within two pixels, which is $125\mu\text{m}$. From table 2, the CT registration error is $16.48\mu\text{m}$ on average. Thus, points in the CT volume located in the build images should be accurate to within $141.48\mu\text{m}$ in the worst case.

4.1 Build Image Registration

Layer-wise build imagery for each part was registered using the algorithm presented in Section 3.1. In our case the perspective is the same for all images, so we can optimize a homography on one image and apply that same homography to all other images. This is important because some images are taken prior to the laser scan and have no visible parts for optimization. The error metric used to align the images was a sum of squared differences between image intensities, which is not reported because it has little physical meaning. Only a qualitative analysis

can be given because we do not know with certainty where the edges of the part are in the build images. Figures 11, 12, 13, and 14 (left) show a layer of each part with the initial alignment overlaid in red and the optimized alignment overlaid in blue. The initial alignment was obtained from four user specified point correspondences in the image and vector data.

All four parts show significant improvement; however, there are a few challenges. First, when attempting to find a single homography for the entire build area, the nonlinear image distortion caused by the lens becomes an issue. Currently we do not account for image distortion due to nonlinear lens effects, which may be the cause of some of the (blue) contour error visible in figures 11, 12, 13, and 14 (left). This could be mitigated by optimizing each part separately or by incorporating distortion parameters into the optimization. Second, the image used for optimization should have high pixel intensity variance inside the part and low variance outside the part. This means that certain views may not be suitable for optimization. For this work we used the post laser scan top view shown in the bottom right of figure 10.

4.2 CT Registration

CT volumes for each part were registered using the algorithm presented in Section 3.2 with one important note. When removing parts from the build plate, some of the material on the bottom surface is lost, which means it no longer corresponds to the laser vectors. To account for this, points on the surface of the CT that interfaced with the build plate are not optimized.

Figures 11, 12, 13, and 14 (right) show the registered CT data. In this illustration, the surface points of each part are color-coded according to their distance as indicated by the TSDF. Blue regions indicate subtractive error, whereas yellow-red regions indicate additive error. Because the TSDF contains physical distances, we can quantify the average distance of the CT surface to the laser vector surface by taking the average TSDF magnitude of all CT surface points. Table 2 presents this error for each part. A higher error indicates many points far away from the vector model, and a low error indicates many points close to the vector model.

Table 2: Registration error for four CT volumes from the sensor test build.

Part	Error (μm)
Nominal Parameter Cylinder	14.9
V+20 Parameter Cylinder	9.8
O2 Fin	10.1
L2 Fin	31.1

The error for the L2 Fin is noticeably larger than the other parts due to post build distortion of the fin. This is also visible in Figure 14 where the fin has large errors at the top and bottom because the rigid transformation does not account for the distortion. It is important to note that this error is due to a discrepancy between the two measurements based on when they were taken. Measurements taken in situ are prior to any deformation, whereas post build measurements include the deformation. Another source of error is due to reflections in the CT volume, which cause erroneous high density returns that are reported as additive error. This is visible in figures 11 and 12 (right) where the stairs meet the large fin on the parameter cylinders.

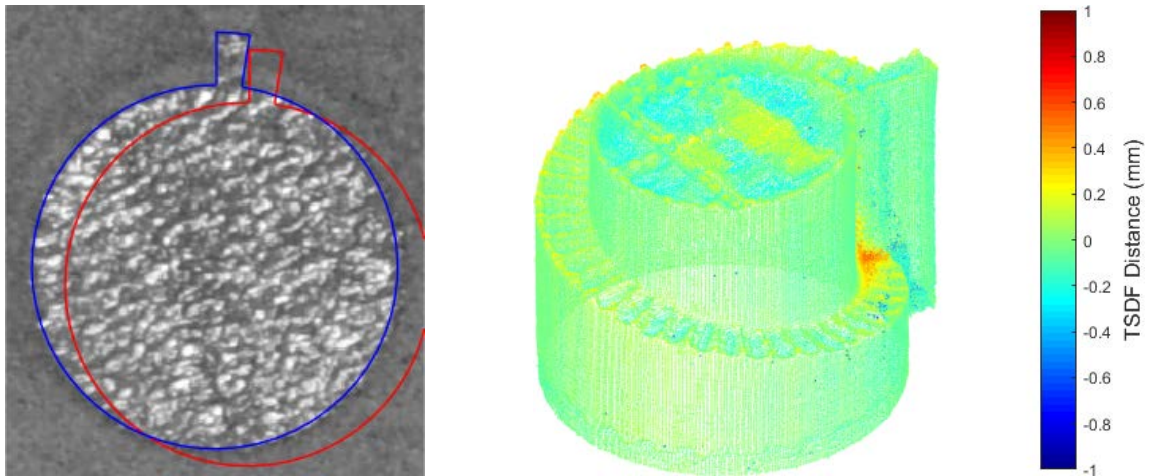


Figure 11: Nominal parameter cylinder build image registration (left). Red lines indicate initial registration and blue lines indicate final registration. CT registration colored by TSDF distance (right).

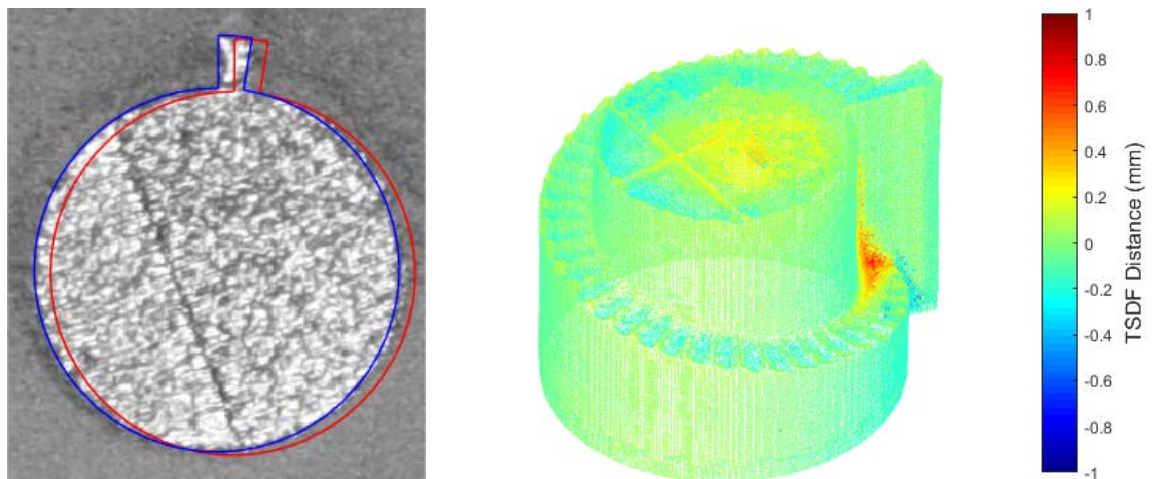


Figure 12: V+20 parameter cylinder build image registration (left). Red lines indicate initial registration and blue lines indicate final registration. CT registration colored by TSDF distance (right).

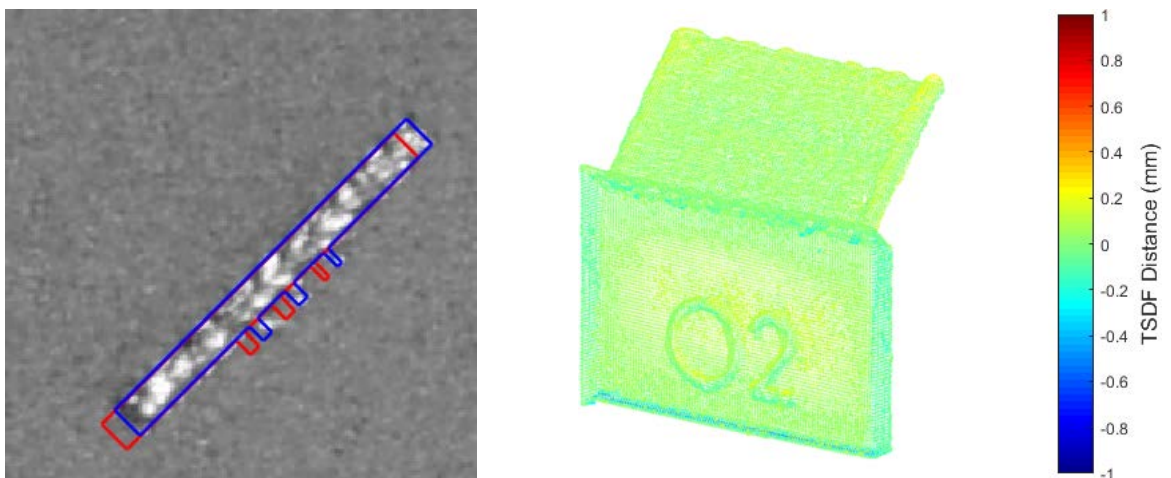


Figure 13: O2 fin build image registration (left). Red lines indicate initial registration and blue lines indicate final registration. CT registration colored by TSDF distance (right).

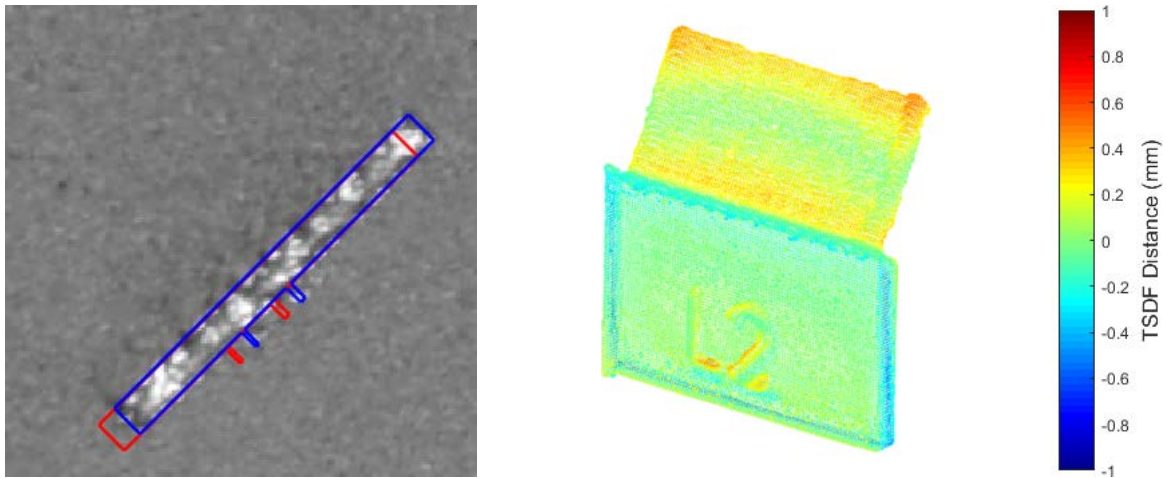


Figure 14: L2 fin build image registration (left). Red lines indicate initial registration and blue lines indicate final registration. CT registration colored by TSDF distance (right).

5. Conclusion

This work presents a methodology for choosing an imaging system to capture the build area at an oblique angle and for registering multiple data modalities associated with the PBFAM process. Registering all data modalities to a single coordinate frame of reference is a required precursor for fault detection and analysis because it allows us to relate machine instructions to real-world process observations. In the future we intend to use flaws readily detectable in the CT volume data correlated to locations in the layer-wise build imagery as positive defect examples for training automated fault detection algorithms. These trained fault detection algorithms would work solely on the layer-wise build imagery, so in-process fault detection will be a reality. Additionally, the algorithms presented in this paper are extensible to other sensing modalities such as thermal imaging.

Future work for improving the registration accuracy would involve improving the system models for both imaging and CT. The current model for the build image registration does not take into account the distortion of the lens. The registration accuracy could be improved by adding distortion parameters to the transformation model. Similarly, the CT registration does not take into account any physical distortion of the part that occurs post build, which is known to occur due to thermal effects. While the rigid alignment allows us to observe the post build distortion, in order to obtain a more accurate mapping of CT to build images the non-rigid transformation needs to be modeled.

Acknowledgements

The authors would like to thank Frederik Verbist, Jan Tops, and Jared Blecher of 3D Systems for their contributions. This material is based in part upon work supported by the Naval Air Systems Command (NAVAIR) under Contract No. N00024-12-D-6404, Delivery Order 0321, as well as by research sponsored by the Air Force Research Laboratory under agreement number

FA8650-12-2-7230. The U.S. Government is authorized to reproduce and distribute reprints for Governmental purposes notwithstanding any copyright notation thereon. Funding for Jacob Morgan was provided through the Applied Research Lab Distinguished Undergraduate Research Program.

Any opinions, findings and conclusions or recommendations expressed in this material are those of the authors and do not necessarily reflect the views of the Naval Air Systems Command (NAVAIR), the Air Force Research Laboratory, or the U.S. Government.

References

- [1] Wegner, A., and G. Witt. "Process monitoring in laser sintering using thermal imaging." *SFF Symposium, Austin, Texas, USA*. 2011.
- [2] Rodriguez, Emmanuel, et al. "Integration of a thermal imaging feedback control system in electron beam melting." *Proceedings of the Solid Freeform Fabrication Symposium*. 2012.
- [3] Doubenskaia, M., et al. "Comprehensive Optical Monitoring of Selective Laser Melting." *Journal of Laser Micro/Nanoengineering* 7.3 (2012).
- [4] zur Jacobsmühlen, Joschka, et al. "High resolution imaging for inspection of laser beam melting systems." *Instrumentation and Measurement Technology Conference (I2MTC), 2013 IEEE International*. IEEE, 2013.
- [5] Tapia, Gustavo, and Alaa Elwany. "A review on process monitoring and control in metal-based additive manufacturing." *Journal of Manufacturing Science and Engineering* 136.6 (2014): 060801.
- [6] Hecht, Eugene. "Optics, 4th." *International edition, Addison-Wesley, San Francisco* 3 (2002).
- [7] Merklinger, Harold M. "Focusing the view camera." *Seaboard Printing Limited* 5 (1996).
- [8] National Electrical Manufacturers Association. *Digital imaging and communications in medicine (DICOM)*. NEMA, 2009.
- [9] Hartley, Richard, and Andrew Zisserman. *Multiple view geometry in computer vision*. Cambridge university press, 2003.
- [10] Moré, Jorge J. "The Levenberg-Marquardt algorithm: implementation and theory." *Numerical analysis*. Springer, Berlin, Heidelberg, 1978. 105-116.
- [11] Baker, Simon, and Iain Matthews. "Lucas-kanade 20 years on: A unifying framework." *International journal of computer vision* 56.3 (2004): 221-255.

- [12] Murray, Richard M., et al. *A mathematical introduction to robotic manipulation*. CRC press, 1994.
- [13] Besl, Paul J., and Neil D. McKay. "Method for registration of 3-D shapes." *Robotics-DL tentative*. International Society for Optics and Photonics, 1992.
- [14] Canelhas, Daniel R., Todor Stoyanov, and Achim J. Lilienthal. "SDF Tracker: A parallel algorithm for on-line pose estimation and scene reconstruction from depth images." *Intelligent Robots and Systems (IROS), 2013 IEEE/RSJ International Conference on*. IEEE, 2013.
- [15] Zhao, Hongkai. "A fast sweeping method for eikonal equations." *Mathematics of computation* 74.250 (2005): 603-627.
- [16] Umeyama, Shinji. "Least-squares estimation of transformation parameters between two point patterns." *IEEE Transactions on pattern analysis and machine intelligence* 13.4 (1991): 376-380.
- [17] Foster, B. K., et al. "Optical, layerwise monitoring of powder bed fusion." *26th International Solid Freeform Fabrication Symposium*; Austin, TX. 2015.